



1 Ground based characterization of spectral optical properties of haze and
2 Asian dust episodes under Asian continental outflow during winter 2014

3

4 Jinsang Jung^{a,*}, JeongAh Yu^b, Youngsook Lyu^b, Minhee Lee^b, Taekyung Hwang^b, Sangil
5 Lee^a

6

7 ^aCenter for Gas Analysis, Korea Research Institute of Standards and Science (KRISS),
8 Daejeon 34113, Republic of Korea

9 ^bDepartment of Climate and Air Quality Research, National Institute of Environmental
10 Research, Daejeon 34944, Republic of Korea

11

12

13 Running title: Optical properties in Daejeon

14

15 Last modified: November 23, 2016

16 Will be submitted to *Atmospheric Chemistry and Physics*

17

18 *Corresponding author: Jinsang Jung (jsjung@kriss.re.kr)

19



Abstract

An intensive field campaign was conducted in a downwind area of the Asian continental outflow (Daejeon, Korea) during winter 2014 to characterize the spectral optical properties of severe haze and Asian dust episodes. High concentrations of PM_{10} (particulate matter with a diameter $\leq 10 \mu\text{m}$) and light scattering coefficients at 550 nm, $\sigma_{s,550}$, were observed during a long-range transport (LRT) haze episode ($\text{PM}_{10} = 163.9 \pm 25.0 \mu\text{g}/\text{m}^3$; $\sigma_{s,550} = 503.4 \pm 60.5 \text{ Mm}^{-1}$) and Asian dust episode ($\text{PM}_{10} = 211.3 \pm 57.5 \mu\text{g}/\text{m}^3$; $\sigma_{s,550} = 560.9 \pm 151 \text{ Mm}^{-1}$). During the LRT haze episode, no significant change in the relative contribution of $\text{PM}_{2.5}$ (particulate matter with a diameter $\leq 2.5 \mu\text{m}$) chemical components was observed as particles accumulated under stagnant atmospheric conditions (January 13–17, 2014), suggesting that the increase in $\text{PM}_{2.5}$ mass concentration was caused mainly by the accumulation of LRT pollutants. On the other hand, a gradual decrease in Ångström exponent (\AA), gradual increase in single scattering albedo (ω) and mass scattering efficiency (MSE) were observed during the stagnant period, possibly due to an increase in particle size. During the Asian dust episode, a low $\text{PM}_{2.5}/\text{PM}_{10}$ ratio and $\text{\AA}(450/700)$ were observed with average values of 0.59 ± 0.06 and 1.08 ± 0.14 , respectively, which were higher than those during the LRT haze episode (0.75 ± 0.06 and 1.39 ± 0.05 , respectively), indicating that $\text{PM}_{2.5}/\text{PM}_{10}$ mass ratios and $\text{\AA}(450/700)$ can be used as tracers to distinguish aged LRT haze and Asian dust under the Asian continental outflow.



41 1. Introduction

42 The optical property of aerosol particles is a very important parameter to understand
43 the aerosol effects on radiative forcing and climate change. Spatiotemporal distributions
44 of aerosol particles are needed to accurately calculate radiative forcing in the global
45 climate system (Li et al., 2016). Atmospheric chemical transport models (CTM) are
46 useful tools for estimating the spatial distributions and concentrations of aerosol
47 particles on regional to global scales. In addition to CTMs, satellite remote sensing is
48 widely used to characterize aerosol particles and their impact on climate change and air
49 quality (van Donkelaar et al., 2010). However, both methods are uncertain due to lack
50 of regional specific optical properties. Thus, to improve the accuracy of CTMs and
51 satellite remote sensing, it is essential to validate these approaches using ground-based
52 remote sensing techniques and surface optical measurements.

53 Severe haze over China can influence the air quality of downwind areas of the Asian
54 continent and regional environments over the East Asia through long-range transport
55 (LRT) by the prevailing westerly (Aikawa et al., 2010; Jung and Kim, 2011; Kaneyasu
56 et al., 2014; Jung et al., 2015). LRT haze can also affect the regional radiation budget
57 directly by scattering or absorbing solar radiation and indirectly by altering the physical
58 properties of clouds and the efficiency of precipitation (Ramanathan et al., 2007; Gao et
59 al., 2014; Jeong et al., 2014; Jung et al., 2015). Zhang et al. (2007) reported that the
60 Asian pollution outflow influences precipitation over the North Pacific. To investigate
61 the impact of LRT haze on regional environments over downwind areas of the Asian
62 continental outflows, it is necessary to characterize the optical properties of LRT haze.

63 The single scattering albedo (ω) is the key parameter used to determine the aerosol
64 effect on radiative forcing and climate change (IPCC, 2013). Thus, accurate



65 measurements of scattering and absorption properties of aerosol particles are important
66 for the better estimation of aerosol radiative forcing. Spectral ω and the backscattering
67 ratio, defined as the ratio of light scattered in the backward hemisphere to the total light
68 scattered, also provide information for the accurate determination of aerosol radiative
69 forcing (Gopal et al., 2014). However, *in situ* observations of spectral aerosol optical
70 properties under Asian continental outflows are rare; thus, an intensive characterization
71 of aerosol optical properties is needed.

72 In Shanghai, China, the ω measured at the surface shows a weak seasonal variation
73 whereas a ground-based remote sensing technique shows the highest ω during the fall
74 season. The ω measured by ground-based remote sensing (0.9–0.93) is ~10 % higher
75 than values measured at the surface (0.8–0.9) (Cheng et al., 2015). From one year's
76 worth of observations in Seoul, Korea, a trend of increasing ω with wavelength was
77 observed during Asian dust events whereas little spectral dependence of ω was observed
78 during LRT haze events (Jung et al., 2010). During the Campaign of Air Quality
79 Research in Beijing 2006 (CAREBeijing-2006), ω was found to be closely related to the
80 inflow of air to Beijing. Relatively low ω (<0.8) was observed for the air mass
81 originated from the north of Beijing whereas relatively high ω was observed for the air
82 mass originated from the south of Beijing (Garland et al., 2009).

83 The objective of this study is to characterize the spectral optical properties of the
84 LRT haze and Asian dust originating from the Asian continent during winter 2014.
85 Integrated chemical and optical measurements of aerosol particles were carried out at
86 Daejeon, Korea during January 2014 to characterize the optical properties of different
87 types of haze. Temporal variations in spectral optical properties under stagnant



88 atmospheric conditions are discussed with reference to aerosol chemical composition.
89 From identified Asian continental outflows, we also investigated the wavelength
90 dependence of aerosol optical properties.

91

92 2. Experimental Methods

93 2.1 Measurement site

94 Online measurements of aerosol optical properties and daily $PM_{2.5}$ (particulate
95 matter with a diameter $\leq 2.5 \mu m$) sampling were conducted at an air quality monitoring
96 station in the mega-city of Daejeon, central Korea (36.19°N, 127.24°E) during January
97 8–31, 2014 (Fig. 1). Because Daejeon is located downwind of Asian continental
98 outflows, it is frequently affected by long-range transported pollutants and Asian dust
99 (Jung et al., 2016). Light scattering and absorption coefficients were continuously
100 measured inside a monitoring building (~15 m above the ground) of the National
101 Institute of Environmental Research in Korea. $PM_{2.5}$ samples were collected on pre-
102 baked quartz fiber filters (Pall-Life Sciences, 47 mm diameter) at a flow rate of 16.7 L
103 min^{-1} . An aerosol sampler (APM Korea, model PMS-103) was installed on the rooftop
104 of the monitoring building. Before and after sampling, filter samples were stored in a
105 freezer at $-20^{\circ}C$ wrapped with aluminum foil. A total of 23 filter samples were
106 collected. Additionally, field blank filters were collected before and after the sampling
107 period. Hourly precipitation data were obtained from a nearby weather monitoring
108 station of the Korea Meteorological Agency.

109

110 2.2 Online measurement of aerosol chemical composition

111 PM_{10} and $PM_{2.5}$ mass concentrations were measured by a beta-attenuation monitor



112 (Met One Instruments, BAM 1020) with an hourly interval. The detection limit of the
113 beta-attenuation technique is reported as $3.6 \mu\text{g m}^{-3}$ by the manufacturer. Hourly PM_{10}
114 potassium (K) concentrations were continuously measured by X-ray fluorescence (XRF)
115 (Cooper Environmental Service (CES), Model Xact 620). The air samples were
116 introduced through a PM_{10} inlet at a flow rate of 16.7 L min^{-1} and drawn through filter
117 tape. The online Xact 620 monitor was calibrated using thin film standards for each
118 element of interest, which was provided by CES. These standards were manufactured by
119 depositing vapor-phase elements on blank Nuclepore (Micromatter Co.). For a 1 hr time
120 resolution, the minimum detection limit for K has been reported to be 0.81 ng m^{-3} (Park
121 et al., 2014).

122 Online measurements of $\text{PM}_{2.5}$ organic carbon (OC) and elemental carbon (EC)
123 were conducted using a semi-continuous carbon analyzer (Sunset Laboratory Inc.,
124 Model RT3140) based on the thermal-optical transmittance (TOT) protocol for
125 pyrolysis correction and the NIOSH (National Institute for Occupational Safety and
126 Health) 5040 method temperature profile (Birch and Cary, 1996; Jung et al., 2010).
127 Measurement condition of the carbon analyzer was described in detail by Jung et al.
128 (2016). The detection limit of both OC and EC was $0.5 \mu\text{g C m}^{-3}$ for 1 hr time
129 resolution, as reported by the manufacturer. The uncertainty of OC and EC
130 measurements has been reported to be 5% (Polidori et al., 2006).

131

132 2.3 Online measurement of aerosol optical properties

133 Light scattering coefficients (σ_s) and hemispheric backscattering coefficients (σ_{bs})
134 of aerosol particles at three wavelengths ($\lambda = 450, 550, \text{ and } 700 \text{ nm}$) were continuously
135 measured using an integrating nephelometer (TSI inc., model 3563). The nephelometer



136 was operated at a flow rate of 5 L min^{-1} with a 5-min averaging time. The clean air and
137 span gas (pure CO_2) calibrations were carried out every hour and once a month,
138 respectively. The uncertainty of the nephelometer measurements was determined to be
139 less than 2% with a 5-min interval. For a 5-min resolution, the detection limits of σ_s
140 were determined to be 6, 3, and 3 Mm^{-1} at 450, 550, and 700 nm, respectively,
141 calculated as 3σ of the clean air measurement. Systematic biases caused by angular
142 truncation errors and a non-Lambertian light source were corrected for scattering
143 measurement data using the the Ångström exponents of σ_s (Anderson et al., 1996;
144 Anderson and Ogren, 1998; Garland et al., 2009). The corrected systematic biases were
145 $\sim 12\%$ of the measured values. The relative humidity (RH) of the sampled air inside the
146 nephelometer chamber was $21 \pm 10\%$.

147 The optical attenuation coefficients (σ_{ATN}) of aerosol particles were measured using
148 the Aethalometer (Magee Scientific, Model AE31) at seven wavelengths (370, 470, 520,
149 590, 660, 880, and 950 nm) (Hansen, 2005). Air samples were drawn through the $\text{PM}_{2.5}$
150 cyclone (BGI Inc., SCC1.829) at a flow rate of 4 L min^{-1} . The light absorption
151 coefficient (σ_a) was retrieved from σ_{ATN} as described by Jung et al. (2010), by
152 considering the “shadowing effect” and multiple scattering within the filter. The
153 detection limit of the aethalometer σ_a , defined as 3σ of the dynamic blank, was
154 determined to be 2 Mm^{-1} . The measurement uncertainty of the Aethalometer is reported
155 to be $\pm 5\%$ by the manufacturer (Hansen, 2005).

156

157 2.4 Chemical analysis of filter samples

158 A quarter of each filter sample was extracted with 10 mL of ultrapure water under



159 ultrasonication (for 30 min). Water extracts were then passed through a disk filter
160 (Millipore, Millex-GV, 0.45 mm) to remove filter debris and water-insoluble particles.
161 Water extracts were stored in a refrigerator at 4 °C prior to analysis. The total organic
162 carbon (TOC) level of the ultrapure water was maintained below 4 ppb using a Labpure
163 S1 filter and an ultraviolet (UV) lamp (ELGA, PureLab Ultra).

164 Water-soluble inorganic ions were analyzed using an ion chromatograph (Thermo
165 Fisher Scientific, Dionex ICS-15000). Analytical conditions of anions (Cl^- , NO_3^- , SO_4^{2-})
166 and cations (Na^+ , NH_4^+ , K^+ , Ca^{2+} , Mg^{2+}) were described in detail by Jung et al. (2016).
167 The detection limits of Cl^- , NO_3^- , and SO_4^{2-} , which are defined as 3 times the standard
168 deviation of field blanks, were determined to be 0.02, 0.01 and 0.11 $\mu\text{g m}^{-3}$, respectively.
169 The analytical error of Cl^- , NO_3^- and SO_4^{2-} measurements was 2.0%, 1.7%, and 2.3%,
170 respectively. The detection limits of NH_4^+ and K^+ were determined to be 0.03 and 0.006
171 $\mu\text{g m}^{-3}$, respectively. The analytical errors of NH_4^+ and K^+ were determined to be 1.4%
172 and 0.73%, respectively.

173

174 2.5 Satellite RGB images and air mass backward trajectories

175 Moderate Resolution Imaging Spectro-radiometer (MODIS) satellite images were
176 obtained from the NASA/MODIS web site (<https://modis.gsfc.nasa.gov/>). Air mass
177 backward trajectories ending at the measurement site were calculated for heights of 200,
178 500 and 1000 m above ground level (AGL) using the HYSPLIT (HYbrid Single-
179 Particle Lagrangian Trajectory) model (Draxler and Rolph, 2016; Rolph, 2016). All
180 back trajectories were ended at 00:00 UTC and 12:00 UTC (09:00 LT and 21:00 LT,
181 respectively) and extended 96 hr backwards.



182

183 2.6 Intensive optical properties

184 2.6.1 Å ngström exponent of aerosol light scattering

185 The wavelength dependent aerosol scattering can be expressed by a power law
 186 (Å ngström, 1929) as follows:

$$187 \quad \sigma_{s,\lambda} = \sigma_{s,\lambda_r} \left(\frac{\lambda}{\lambda_r} \right)^{-\tilde{A}} \quad (1)$$

188 where σ_{s,λ_r} is the scattering coefficient at a reference wavelength λ_r and \tilde{A} is the
 189 Å ngström exponent. The Å ngström exponent can be retrieved from the slope of a
 190 double-logarithmic plot of σ_s versus λ as follows:

$$191 \quad \tilde{A} \left(\frac{\lambda_1}{\lambda_2} \right) = - \frac{\log \left(\frac{\sigma_{s,\lambda_1}}{\sigma_{s,\lambda_2}} \right)}{\log \left(\frac{\lambda_1}{\lambda_2} \right)} \quad (2)$$

192

193 2.6.2 Backscattering fraction, single scattering albedo, and mass scattering efficiency

194 The backscattering coefficient is defined as the scattered light intensity in the
 195 backward hemisphere of the particle (90°–180°) (Anderson and Ogren, 1998). The
 196 backscattering ratio is used to derive the slope of the particle size distribution and also
 197 provides an estimate of the bulk refractive index of particles in the atmosphere (Gopal et
 198 al., 2014). The hemispheric backscattering fraction, b_λ , is defined as the ratio of the
 199 backscattering coefficient to the total scattering coefficient at a given wavelength ($\lambda =$
 200 450, 550, and 700 nm), calculated as

$$201 \quad b_\lambda = \frac{\sigma_{bs,\lambda}}{\sigma_{s,\lambda}} \quad (3)$$

202 The single scattering albedo, ω_λ , is the ratio of the scattering coefficient to the
 203 extinction coefficient at a given wavelength. Here, ω_λ at a certain λ can be calculated as



204 follows:

$$205 \quad \omega_{\lambda} = \frac{\sigma_{s,\lambda}}{\sigma_{s,\lambda} + \sigma_{a,\lambda}} \quad (4)$$

206 Because σ_a was not measured at 550 nm by an aethalometer, σ_a at $\lambda = 520$ nm is
 207 converted to σ_a at $\lambda = 550$ nm as follows:

$$208 \quad \sigma_{a,500} = \sigma_{a,520} * \left(\frac{\lambda(550 \text{ nm})}{\lambda(520 \text{ nm})} \right)^{-\alpha} \quad (5)$$

209 where α is the absorbing Ångström exponent, which was determined from spectral
 210 aerosol light absorption as follows:

$$211 \quad \alpha = - \frac{\log(\sigma_{a,590}) - \log(\sigma_{a,520})}{\log(590 \text{ nm}) - \log(520 \text{ nm})} \quad (6)$$

212 The mass scattering efficiency, MSE_{λ} , is the ratio of the scattering coefficient to the
 213 mass concentrations at a given wavelength, expressed as

$$214 \quad MSE_{\lambda} = \frac{\sigma_{s,\lambda}}{PM_{2.5} \text{ mass}} \quad (7)$$

215

216 3. Results and Discussion

217 3.1 Temporal variations in PM mass and light scattering coefficient (σ_s)

218 Figure 2 shows temporal variations in wind speed and hourly precipitation, PM_{10} and
 219 $PM_{2.5}$ mass, the $PM_{2.5}/PM_{10}$ mass ratio, and the light scattering coefficient (σ_s) at the
 220 measurement site in Daejeon during January 8–31, 2014. The PM_{10} mass concentrations
 221 ranged from 19 to 270 $\mu\text{g m}^{-3}$ with an average of $83 \pm 42 \mu\text{g m}^{-3}$, and $PM_{2.5}$ mass
 222 concentrations ranged from 8 to 147 $\mu\text{g m}^{-3}$ with an average of $57 \pm 30 \mu\text{g m}^{-3}$ during
 223 the measurement period. The average $PM_{2.5}$ mass concentration in this study is much
 224 higher than the US EPA NAAQS (National Ambient Air Quality Standards) for $PM_{2.5}$ of
 225 35 $\mu\text{g m}^{-3}$ (24 hr average). Average $PM_{2.5}/PM_{10}$ mass ratios ranged from 0.41 to 0.93



with an average of 0.68 ± 0.1 . σ_s at 550 nm ranged from 12.7 to 678.4 Mm^{-1} with an average of $189.1 \pm 142.0 \text{ Mm}^{-1}$. The average σ_s in this study is comparable with the annual mean of 217 Mm^{-1} measured in the Shanghai region, China during 2010–2012 (Cheng et al., 2015) but is lower than the annual mean of 360 Mm^{-1} in the Beijing region, China measured during 2009–2010 (Jing et al., 2015). Because light scattering is caused mainly by aerosol particles and the scattering measurements of the present study were performed under dry conditions ($\text{RH} < 30\%$), similar temporal patterns were observed for PM mass and σ_s (Fig. 2).

As shown in Fig. 2, three haze episodes were observed on 12, 17, and 20 January 2014 with peak PM_{10} mass concentrations of 173, 210, and 270 $\mu\text{g m}^{-3}$, respectively. $\text{PM}_{2.5}/\text{PM}_{10}$ mass ratios during the episodes were measured as 0.71, 0.69, and 0.54, respectively, during the three episodes. The first and second haze episodes were caused mainly by the accumulation of pollutants for 3–4 days under stagnant atmospheric conditions with relatively low wind speed (Fig. 2). After 3–4 days of aerosol accumulation, PM mass concentrations showed a sharp decrease with relatively high wind speeds ($> 2 \text{ m/sec}$). A sharp increase in PM_{10} mass was observed during the third episode when a relatively high wind speed was observed (Fig. 2a). A similar temporal pattern was observed for σ_s and PM_{10} mass concentrations during the three haze episodes. The light scattering coefficient at 550 nm reached peak values of 494.2, 594.4, and 678.4 Mm^{-1} during the first, second, and third episodes, respectively (Fig. 2d).

During the first and second haze episodes, no precipitation was observed whereas before and after the third haze episode light precipitation was observed with an hourly average of 0.5–1.5 mm/hr. Sharp decrease of σ_s and PM_{10} mass concentrations during the third haze episode was mainly attributed to precipitation. However, the first and



250 second haze episodes were not influenced by precipitation.

251

252 3.2 Single scattering albedo (ω), Ångström exponent (\AA), and backscattering fraction
 253 (b)

254 Figure 3 shows temporal variations in aerosol optical properties, including σ_s , \AA ,
 255 backscattering fraction (b), and ω . The \AA value between 450 and 700 nm ($\text{\AA}(450/700)$)
 256 ranged from 0.94 to 1.99 with an average of 1.60 ± 0.19 , which is comparable to the
 257 $\text{\AA}(450/550)$ value of 1.59 ± 0.21 and $\text{\AA}(550/700)$ value of 1.61 ± 0.19 listed in Table 1.
 258 The $\text{\AA}(450/700)$ value obtained in this study is slightly higher than that obtained in
 259 Beijing, China during summer 2006 (1.42 ± 0.19 ; Garland et al., 2009) and that
 260 obtained in Guangzhou, China during summer 2006 (1.51 ± 0.20 ; Garland et al., 2008).
 261 Because \AA is negatively correlated with particle diameter (Eck et al., 1999), the slightly
 262 higher \AA observed in this study compared with those from Mainland China implies
 263 larger aerosol particles in this study.

264 During the measurement period, b at 550 nm (b_{550}) ranged from 0.08 to 0.17 with an
 265 average of 0.12 ± 0.02 , which is comparable with b_{450} (0.12 ± 0.02) but slightly lower
 266 than b_{700} (0.15 ± 0.02). Similar patterns of b with wavelength were observed in Beijing
 267 owing to a decrease in particle size with increasing wavelength (Garland et al., 2009).
 268 The ω at 550 nm (ω_{550}) ranged from 0.58 to 0.95 with an average of 0.85 ± 0.07 , which
 269 is comparable with ω_{450} (0.85 ± 0.07) and ω_{700} (0.84 ± 0.08). The average ω_{550} is close
 270 to the values reported from other locations in and around Beijing and Guangzhou (ω_{550}
 271 = 0.82–0.85) (Bergin et al., 2001; Andreae et al., 2008; Cheng et al., 2008; Garland et
 272 al., 2008, 2009).

273 Dynamic temporal patterns in \AA , b , and ω were observed during the measurement



274 period (Fig. 3). Gradual decreases in \dot{A} with increasing σ_s were observed during the first
 275 and second haze episodes, whereas a sharp decrease in \dot{A} was observed with increasing
 276 σ_s during the third episode. It was also found that b was negatively correlated with σ_s
 277 during the three episodes. Meanwhile, ω increased gradually with σ_s during the first and
 278 second episodes. These results indicate that temporal variations in \dot{A} , b , and ω are
 279 closely related to those in σ_s . In this study, \dot{A} and b were negatively correlated with σ_s
 280 whereas ω was positively correlated with σ_s .

281 Figure 4 clearly shows that ω_{550} increases with $\sigma_{s,550}$. When ω_{550} was less than 200
 282 Mm^{-1} , ω_{550} varied widely from 0.6 to >0.9 . The $\dot{A}(450/700)$ value increased with $\sigma_{s,550}$
 283 when $\sigma_{s,550}$ was lower than $\sim 150 \text{ Mm}^{-1}$. However, when $\sigma_{s,550}$ was higher than ~ 150
 284 Mm^{-1} , $\dot{A}(450/700)$ gradually decreased with increasing $\sigma_{s,550}$. Figure 5a shows a scatter
 285 plot of ω_{550} versus b_{550} as a function of $\sigma_{s,550}$, where ω_{550} is observed to decrease as b_{550}
 286 increases. A scatter plot of b_{550} versus $\dot{A}(450/700\text{m})$ is shown in Fig. 5b. A positive
 287 correlation is observed between $\dot{A}(450/700)$ and b_{550} when $\sigma_{s,550}$ is higher than 200 Mm^{-1}
 288 1 , whereas a poor correlation is observed when $\sigma_{s,550}$ is lower than 200 Mm^{-1} . In
 289 addition, a relatively small b_{550} is observed as $\sigma_{s,550}$ increases (Fig. 5a and b).

290

291 3.3 Aerosol optical properties during severe haze episodes

292 3.3.1 Classification of haze episodes

293 As shown in Fig. 2b, three haze episodes were observed during 11–12, 14–17, and 20
 294 January 2014. This study focused on the second and third haze episodes, which peaked
 295 on 17 and 20 January 2014. Figure 6 shows MODIS RGB images during 14–17 January
 296 2014. A dense haze layer is clearly seen over East China during 14 January. This layer
 297 moved slowly to the Korean Peninsula from 15 to 17 January. Air mass backward



trajectories ending at the measurement site also show the transport of air masses from East China to the Korean Peninsula on 17 January 2014, as shown in Fig. 7a. During the second haze episode, very low wind speeds of $<1 \text{ m sec}^{-1}$ were observed (Fig. 2a). Thus, the second haze episode is classified as a period of accumulation of LRT pollutants from the Asian continent (LRT haze).

During the third haze episode on 20 January, very high concentrations of K (maximum: $4.9 \mu\text{g m}^{-3}$, average: $2.2 \pm 2.3 \mu\text{g m}^{-3}$) were observed (Table 2). The air mass backward trajectory for 20 January clearly shows that the air mass originating from the Nei Mongol desert area had an impact on the Korean Peninsula (Fig. 7b). During the third haze episode, relatively high wind speeds of $>2 \text{ m sec}^{-1}$ were observed (Fig. 2a). Thus, the third haze episode is classified as an Asian dust episode.

309

3.3.2 Temporal variations in the chemical and optical properties of LRT haze

Figure 8 shows temporal variations in the chemical composition of $\text{PM}_{2.5}$ during the LRT haze episode (14–17 January 2014). As mentioned above, the LRT haze episode was caused mainly by the accumulation of long-range transported pollutants from the Asian continent. Gradual increases in total $\text{PM}_{2.5}$ mass were observed during the LRT haze episode (Fig. 8a). The relative contribution of $\text{PM}_{2.5}$ chemical composition is also shown in Fig. 8b. Organic aerosol (OA) dominated the $\text{PM}_{2.5}$ mass composition, followed by NO_3^- , SO_4^{2-} and NH_4^+ . Even though a small decrease in OA mass fraction was observed during 15 January, the mass fractions of the major $\text{PM}_{2.5}$ chemical components were invariant from 14 to 17 January. These results suggest that the increase in $\text{PM}_{2.5}$ mass concentration observed during the LRT haze episode was caused mainly by the accumulation of LRT pollutants.



Figure 9 shows temporal variations in the daily average intensive optical properties of the LRT haze. The $\hat{A}(450/700)$ and b_{550} values decreased during the accumulation period from 14 to 17 January while MSE_{550} and ω_{550} increased. Average $\hat{A}(450/700)$ decreased from 1.74 ± 0.09 on 14 January to 1.39 ± 0.05 on 17 January. Average b_{550} decreased from 0.15 ± 0.01 on 14 January to 0.10 ± 0.003 on 17 January. Average MSE_{550} of PM_{10} increased from $1.73 \pm 0.40 \text{ m}^2 \text{ g}^{-1}$ on 14 January to $3.11 \pm 0.46 \text{ m}^2 \text{ g}^{-1}$ on 17 January. An increase in MSE_{550} with increasing PM mass concentration during the haze episodes was also observed in Beijing and Guangzhou, China during summer 2006 (Jung et al., 2009a, b). For example, in Beijing the MSE_{550} of PM_{10} increased from $1.4 \pm 0.89 \text{ m}^2 \text{ g}^{-1}$ during relatively clean conditions to $3.1 \pm 0.9 \text{ m}^2 \text{ g}^{-1}$ during relatively polluted conditions (Jung et al., 2009a). At most monitoring sites in the United States, dry MSE increased with increasing mass concentration (IMPROVE, 2006).

Average ω_{550} increased from 0.81 ± 0.07 on 14 January to 0.90 ± 0.03 on 17 January. A similar pattern was observed as pollution increased in Beijing during summer 2006 (Jung et al., 2009a). Average ω_{550} increased from ~ 0.75 during relatively clean conditions to ~ 0.86 during relatively polluted conditions in Beijing during summer 2006 owing to an increase in SO_4^{2-} , NO_3^- , NH_4^+ , and organic aerosols (Jung et al., 2009a). Because EC is a strong light-absorbing aerosol, changes in EC mass fraction in $PM_{2.5}$ mass can be used as an indicator of ω . As shown in Fig. 8b, EC mass fraction in $PM_{2.5}$ was invariant from 14 to 17 January. These results indicate that an increase in mass concentration of secondary aerosols such as SO_4^{2-} , NO_3^- , NH_4^+ , and secondary organic aerosol cannot explain the increase in ω_{550} under stagnant conditions during the LRT haze episode. On the other hand, an increase in MSE_{550} under stagnant



conditions (Fig. 9b) can enhance ω_{550} , resulting in an increase in ω_{550} under stagnant conditions.

The amount of light scattered by aerosol particles can be accurately estimated using Mie theory when the size distribution and refractive index of the particles are known (Mie, 1908; Hess et al., 1998; Seinfeld and Pandis, 1998). Light scattering efficiencies of $(\text{NH}_4)_2\text{SO}_4$ and organic aerosols at 550 nm were calculated using Mie theory using refractive indices for $1.53-0i$ and $1.55-0i$, respectively (Liu et al., 2009), as shown in Fig. 10. Light scattering efficiencies of $(\text{NH}_4)_2\text{SO}_4$ and organic aerosols at 550 nm increase as particle size increases to 600 nm.

Freshly formed aerosol particles have a diameter (D_p) of less than 100 nm (Yue et al., 2010) and grow into the accumulation mode ($100 \text{ nm} < D_p < 1000 \text{ nm}$) through the condensation of gas vapors or coagulation (collisions between particles; Seinfeld and Pandis, 1998). Thus, larger particles (in the accumulation mode) are observed under polluted stagnant conditions. An increase in D_p under stagnant conditions can enhance light scattering, resulting in an increase in MSE . \tilde{A} and b are also closely related to the size of aerosol particles. For example, Eck et al. (1999) reported that coarse mode particles had relatively low \tilde{A} compared with fine mode particles. Nemessure et al. (1995) reported that the forward scattering fraction increases as particle size increases, resulting in a decrease in b . This suggests that the temporal variations in intensive optical properties shown in Fig. 9 are closely related to the change in size of aerosol particles under stagnant conditions.

367

3.3.3 Inter-comparison of the aerosol optical properties of LTP haze versus Asian dust particles



370 Optical properties of the LRT haze and Asian dust are compared in Fig. 11 and
371 summarized in Table 2. For this comparison, data obtained on 17 January were used to
372 represent aged LRT haze. Elevated K concentrations were observed during the Asian
373 dust episode, with an average of $2.2 \pm 2.3 \mu\text{g m}^{-3}$. Similar levels of $\text{PM}_{2.5}$ mass were
374 obtained during the LRT haze and Asian dust episodes, whereas much higher PM_{10}
375 mass was obtained during the Asian dust episode compared with the LRT haze episode
376 (Table 2), resulting in higher $\text{PM}_{2.5}/\text{PM}_{10}$ mass ratios during the LRT haze episode (0.75
377 ± 0.0) compared with the Asian dust episode (0.59 ± 0.06). Higher EC/PM_{10} mass ratios
378 were observed during the LRT haze episode with an average of 0.033 ± 0.00 compared
379 with the Asian dust episode (0.026 ± 0.003). $\text{PM}_{2.5}/\text{PM}_{10}$ mass ratios and EC/PM_{10} mass
380 ratios during the Asian dust episode were higher than those obtained in Seoul, Korea
381 during severe Asian dust episodes in 2007–2008 ($\text{PM}_{2.5}/\text{PM}_{10} < 0.4$; $\text{EC}/\text{PM}_{10} < 0.013$).
382 In addition, high $\text{PM}_{2.5}$ mass concentrations during the Asian dust episode in this study
383 suggest that Asian dust particles mixed with LRT haze originating from anthropogenic
384 emissions had an impact on the measurement site on 20 January.

385 Similar levels of σ_s were observed during the LRT haze ($503.4 \pm 60.5 \text{ Mm}^{-1}$) and
386 Asian dust episode ($560.9 \pm 151 \text{ Mm}^{-1}$) (Fig. 11a). The ω_{550} values obtained for the two
387 episodes were comparable, with averages of 0.91 ± 0.03 and 0.92 ± 0.0 observed during
388 the LRT haze and Asian dust episodes, respectively. However, a higher light absorption
389 coefficient ($\sigma_{a,550}$) was obtained during the LRT haze episode ($51.9 \pm 21.9 \text{ Mm}^{-1}$)
390 compared with the Asian dust episode ($39.4 \pm 7.3 \text{ Mm}^{-1}$). Higher $\text{\AA}(450/700)$ was
391 obtained during the LRT haze episode (average of 1.39 ± 0.05) compared with the
392 Asian dust episode (1.08 ± 0.14), due mainly to the relatively large size distribution
393 during the Asian dust episode. The results of this study suggest that $\text{PM}_{2.5}/\text{PM}_{10}$ mass



394 ratios and $\text{\AA}(450/700)$ can be used as tracers to distinguish aged LRT haze and Asian
395 dust based on differences in the particle size distribution.

396

397 4. Conclusion

398 An intensive field campaign was conducted at an area downwind of the Asian
399 continental outflow (Daejeon, Korea) during winter 2014 to characterize the spectral
400 optical properties of severe haze episodes. Dynamic temporal patterns of aerosol optical
401 properties were observed during the measurement period. During the stagnant period
402 (January 13–17, 2014), after long-range transport of haze from the Asian continent, no
403 significant change in the mass fraction of $\text{PM}_{2.5}$ chemical composition was observed,
404 with the highest fraction being organic aerosol, followed by NO_3^- , NH_4^+ , and SO_4^{2-} . On
405 the other hand, a gradual decrease in \AA ngström exponent (\AA) and gradual increases in
406 single scattering albedo (ω) and mass scattering efficiency (MSE) were observed during
407 the stagnant period. Mie calculations suggest that the increase in aerosol particle
408 diameter under stagnant conditions enhanced light scattering, resulting in an increase in
409 MSE . It is also suggested that the increase in MSE under stagnant conditions enhanced
410 ω . These results imply that changes in particle size rather than chemical composition
411 during the stagnant period is the dominant factor affecting the aerosol optical properties.

412 During the Asian dust episode, very high values of PM_{10} mass and light scattering
413 coefficient at 550 nm, $\sigma_{s,550}$, were observed with averages of $211.3 \pm 57.5 \mu\text{g m}^{-3}$ and
414 $560.9 \pm 151 \text{ Mm}^{-1}$, respectively. The ω_{550} during the LTP haze and Asian dust episodes
415 were comparable, with averages of 0.91 ± 0.03 and 0.92 ± 0.0 , respectively, implying
416 that aged LRT pollutants and Asian dust particles have similar ω . A relatively small
417 $\text{PM}_{2.5}/\text{PM}_{10}$ ratio and $\text{\AA}(450/700)$ were observed during the Asian dust episode



418 compared with those during the LRT haze episode, indicating that $PM_{2.5}/PM_{10}$ mass
419 ratios and $\text{\AA}(450/700)$ can be used as tracers to distinguish aged LRT haze and Asian
420 dust.

421

422 Acknowledgements

423 This work was conducted by a co-research project of the National Institute of
424 Environmental Research (NIER) and the Korean Research Institute of Standards and
425 Science (KRISS). This study was funded by the Korean Meteorological Administration
426 Research and Development Program under grant KMIPA 2015-5020.

427

428



References

- Aikawa, M., Toshimasa, O., Takatoshi, H., Oishi, O., Tsuji, A., Yamagami, M., Murano, K., and Mukai, H.: Significant geographic gradients in particulate sulfate over Japan determined from multiple-site measurements and a chemical transport model: Impacts of transboundary pollution from the Asian continent, *Atmos. Environ.*, 44, 381–391, 2010.
- Anderson, T. and Ogren, J.: Determining aerosol radiative properties using the TSI 3563 integrating nephelometer, *Aerosol Sci. Technol.*, 29, 57–69, doi:10.1080/02786829808965551, 1998.
- Anderson, T. L., et al.: Performance characteristics of a high sensitivity, three-wavelength, total scatter/backscatter nephelometer, *J. Atmos. Oceanic Technol.*, 13, 967–986, 1996.
- Andreae, M. O., et al.: Optical properties and chemical composition of the atmospheric aerosol in urban Guangzhou, China. *Atmos. Environ.*, 42, 6335–6350, 2008.
- Ångström, A.: On the atmospheric transmission of sun radiation and on dust in the air, *Geogr. Ann.*, 11, 156–166, 1929.
- Bergin, M., et al.: Aerosol radiative, physical, and chemical properties in Beijing during June 1999, *J. Geophys. Res.*, 106, 17,969–17,980, doi:10.1029/2001JD900073, 2001.
- Birch, M. and Cary, R.: Elemental carbon-based method for monitoring occupational exposures to particulate diesel exhaust, *Aerosol Sci. Technol.*, 25, 221–241, 1996.
- Cheng, Y., et al.: Aerosol optical properties and related chemical apportionment at Xinken in Pearl River Delta of China, *Atmos. Environ.*, 42, 6351–6372, 2008.
- Cheng, T., Xu, C., Duan, J., Wang, Y., Leng, C., Tao, J., Che, H., He, Q., Wu, Y., Zhang, R., Li, X., Chen, J., Kong, L., and Yu, X.: Seasonal variation and difference of aerosol optical properties in columnar and surface atmospheres over Shanghai, *Atmos. Environ.*, 123, 315–326, 2015.
- Draxler, R. and Rolph, G.: HYSPLIT (HYbrid Single-Particle Lagrangian Integrated Trajectory) Model access via NOAA ARL READY Website (<http://www.arl.noaa.gov/HYSPLIT.php>), NOAA Air Resources Laboratory, Silver



- Spring, MD, 2016.
- Eck, T., Holben, B., Reid, J., Dubovik, O., Smirnov, A., O'Neill, N., Slutsker, I., and Kinne, S.: Wavelength dependence of the optical depth of biomass burning, urban, and desert dust aerosols, *J. Geophys. Res.*, 104, 31333–31349, 1999.
- Gao, Y., Zhao, C., Liu, X., Zhang, M., and Leung, L.: WRF-Chem simulations of aerosols and anthropogenic aerosol radiative forcing in East Asia, *Atmos. Environ.*, 92, 250–266, 2014.
- Garland, R., et al.: Aerosol optical properties in a rural environment near the mega-city Guangzhou, China: Implications for regional air pollution, radiative forcing and remote sensing, *Atmos. Chem. Phys.*, 8, 5161–5186, 2008.
- Garland, R., Schmid, O., Nowak, A., Achtert, P., Weidensohler, A., Gunthe, S., Tekegawa, N., Kita, K., Kondo, Y., Hu, M., Shao, M., Zeng, L., Zhu, T., Andreae, M., and Pöschl, U.: Aerosol optical properties observed during Campaign of Air Quality Research in Beijing 2006 (CAREBeijing-2006): Characteristic differences between the inflow and outflow of Beijing city air, *J. Geophys. Res.*, 114, D00G04, doi:10.1029/2008JD010780, 2009.
- Gopal, K., Arafath, S., Lingaswamy, A., Balakrishnaiah, G., Kumari, S., Devi, K., Reddy, N., Reddy, K., Reddy, M., Reddy, R., and Babu, S.: In-situ measurements of atmospheric aerosols by using Integrating Nephelometer over a semi-arid station, southern India, *Atmos. Environ.*, 86, 228–240, 2014.
- Hansen, A.: The Aethalometer, manual, Berkeley, California, USA, Magee Scientific, 2005.
- Hess, M., Koepke, P., and Schult, I.: Optical properties of aerosols and clouds: The software package OPAC, *Bull. Am. Met. Soc.*, 79, 831–844, 1998.
- IMPROVE: Spatial and Seasonal Patterns and Temporal Variability of Haze and its Constituents in the United States: Report IV (is available on <http://vista.cira.colostate.edu/improve/Publications/Reports/2000/2000.htm>), 2006.
- IPCC: Summary for policymakers. In: Stocker, T.F., Qin, D., Plattner, G.-K., Tignor, M., Allen, S.K., Boschung, J., Nauels, A., Xia, Y., Bex, V., Midgley, P.M. (Eds.), *Climate Change 2013: the Physical Science Basis. Contribution of Working Group I to the Fifth Assessment Report of the Intergovernmental Panel on Climate Change*, Cambridge, United Kingdom and New York, NY, USA, 2013.



- 492 Jeong, H., Chung, C., van Noije, T., and Takemura, T.: Relationship between fine-mode
 493 AOD and precipitation on seasonal and interannual time scales, *Tellus B*, 66, 23037,
 494 <http://dx.doi.org/10.3402/tellusb.v66.23037>, 2014.
- 495 Jing, J., Wu, Y., Tao, J., Che, H., Xia, X., Zhang, X., Yan, P., Zhao, D., and Zhang, L.:
 496 Observation and analysis of near-surface atmospheric aerosol optical properties in
 497 urban Beijing, *Particuology*, 18, 144–154, 2015.
- 498 Jung, J., Lee, H., Kim, Y., Liu, X., Zhang, Y., Hu, M., and Sugimoto, N.: Optical
 499 Properties of Atmospheric Aerosols Obtained by In-situ and Remote Measurements
 500 during 2006 CAREBEIJING Campaign, *J. Geophys. Res.*, 114, D00G02,
 501 doi:10.1029/2008JD010337, 2009a.
- 502 Jung, J., Lee, H., Kim, Y., Liu, X., Zhang, Y., Gu, J., and Fan, S.: Aerosol chemistry and
 503 the effect of aerosol water content on visibility impairment and radiative forcing in
 504 Guangzhou during the 2006 Pearl River Delta campaign, *J. Environ. Manage.*, 90,
 505 3231–3244, 2009b.
- 506 Jung, J., Kim, Y., Lee, K., Cayetano, M., Batmunkh, T., Koo, J., and Kim, J.: Spectral
 507 optical properties of long-range transport Asian Dust and pollution aerosols over
 508 Northeast Asia in 2007 and 2008, *Atmos. Chem. Phys.*, 10, 5391–5408, 2010.
- 509 Jung, J. and Kim, Y.: Tracking sources of severe haze episodes and their
 510 physicochemical and hygroscopic properties under Asian continental outflow:
 511 Long-range transport pollution, postharvest biomass burning, and Asian dust, *J.*
 512 *Geophys. Res.*, 116, D02206, doi:10.1029/2010JD014555, 2011.
- 513 Jung, J., Lee, K., Cayetano, M., Batmunkh, T., and Kim, Y.: Optical and hygroscopic
 514 properties of long-range transported haze plumes observed at Deokjeok Island off
 515 the west coast of the Korean Peninsula under the Asian continental outflows, *J.*
 516 *Geophys. Res.*, 120, 8861–8877, doi:10.1002/2015JD023154, 2015.
- 517 Jung, J., Lyu, Y., Lee, M., Hwang, T., Lee, S., and Oh, S.: Impact of Siberian forest fires
 518 on the atmosphere over the Korean Peninsula during summer 2014, *Atmos. Chem.*
 519 *Phys.*, 16, 6757–6770, 2016.
- 520 Kaneyasu, N., Yamamoto, S., Sato, K., Takami, A., Hayashi, M., Hara, K., Kawamoto,
 521 K., Okuda, T., and Hatakeyama, S.: Impact of long-range transport of aerosols on
 522 the PM_{2.5} composition at a major metropolitan area in the northern Kyushu area of
 523 Japan, *Atmos. Environ.*, 97, 416–425, 2014.



- 524 Li, S., Yu, C., Chen, L., Tao, J., Letu, H., Ge, W., Si, Y., and Liu, Y.: Inter-comparison of
525 model-simulated and satellite-retrieved componential aerosol optical depths in
526 China, *Atmos. Environ.*, 141, 320–332, 2016.
- 527 Liu, X., Zhang, Y., Jung, J., Gu, J., Li, Y., Guo, S., Chang, S., Yue, D., Lin, P., Kim, Y.,
528 Hu, M., Zeng, L., and Zhu, T.: Research on the hygroscopic properties of aerosols
529 by measurement and modeling during CAREBeijing-2006, *J. Geophys. Res.*, 114,
530 D00G16, doi:10.1029/2008JD010805, 2009.
- 531 Mie, G.: Beiträge zur Optik trüber Medien, speziell kolloidaler Metalllösungen, *Ann.*
532 *Phys.*, 330, 377–445, doi:10.1002/andp.19083300302, 1908.
- 533 Nemasure, S., Wagener, R., and Schwartz, S.: Direct shortwave forcing of climate by
534 the anthropogenic sulfate aerosol: Sensitivity to particle size, composition, and
535 relative humidity, *J. Geophys. Res.*, 100, 26105–26116, 1995.
- 536 Park, S., Cho, S., Jo, M., Gong, B., Park, J., and Lee, S.: Field evaluation of a near-real
537 time elemental monitor and identification of element sources observed at an air
538 monitoring supersite in Korea. *Atmos. Pollut. Res.*, 5, 119–128, 2014.
- 539 Polidori, A., Turpin, B., Lim, H., Cabada, J., Subramanian, R., Pandis, S., and Robinson,
540 A.: Local and Regional Secondary Organic Aerosol: Insights from a Year of Semi-
541 Continuous Carbon Measurements at Pittsburgh, *Aerosol Sci. Technol.*, 40, 861–872,
542 2006.
- 543 Ramanathan, V., Ramana, M., Roberts, G., Kim, D., Corrigan, C., Chung, C., and
544 Winker, D.: Warming trends in Asia amplified by brown cloud solar absorption,
545 *Nature*, 448, doi: 10.1038/nature06019, 2007.
- 546 Rolph, G.: Real-time Environmental Applications and Display sYstem (READY)
547 Website (<http://www.arl.noaa.gov/ready.php>), NOAA Air Resources Laboratory,
548 Silver Spring, MD, 2016.
- 549 Seinfeld, J. and Pandis, S.: *Atmospheric Chemistry and Physics: From Air Pollution to*
550 *Climate Change*, John Wiley, Hoboken, N. J., 1998.
- 551 van Donkelaar, A., Martin, R., Brauer, M., Kahn, R., Levy, R., Verduzco, C., and
552 Villeneuve, P.: Global estimates of ambient fine particulate matter concentrations
553 from satellite-based aerosol optical depth: development and application. *Environ.*
554 *Health Perspect.*, 118, 847–855, 2010.
- 555 Zhang, R., Li, G., Fan, J., Wu, D., and Molina, M.: Intensification of Pacific storm track



556 linked to Asian pollution, Proc. Natl. Acad. Sci., 104, 5295–5299, 2007.

557

558



559 Table 1. Summary of aerosol optical parameters observed in Daejeon, Korea during
 560 January 2014.

Component	Unit	Min–Max (Average \pm S.D.)
Light scattering coefficient,		
$\sigma_{s,450}$	Mm ⁻¹	16.5–805.0 (256.9 \pm 183.7)
$\sigma_{s,550}$	Mm ⁻¹	12.7–678.4 (189.1 \pm 142.0)
$\sigma_{s,700}$	Mm ⁻¹	9.3–531.6 (129.1 \pm 101.3)
Backscattering coefficient,	Mm ⁻¹	
$\sigma_{bs,450}$		2.4–77.2 (27.6 \pm 16.9)
$\sigma_{bs,550}$	Mm ⁻¹	1.7–61.3 (21.3 \pm 13.3)
$\sigma_{bs,700}$	Mm ⁻¹	1.4–57.2 (17.8 \pm 11.7)
Å ngström Exponent of σ_s ,		
Å (450/550)		0.85–2.06 (1.59 \pm 0.21)
Å (450/700)		0.94–1.99 (1.60 \pm 0.19)
Å (550/700)		1.0–1.97 (1.61 \pm 0.19)
Hemispheric backscattering		
fraction, b_{450}		0.08–0.17 (0.12 \pm 0.02)
b_{550}		0.08–0.17 (0.12 \pm 0.02)
b_{700}		0.1–0.19 (0.15 \pm 0.02)
Single scattering albedo, ω_{450}		0.57–0.95 (0.85 \pm 0.07)
ω_{550}		0.58–0.95 (0.85 \pm 0.07)
ω_{700}		0.56–0.95 (0.84 \pm 0.08)

561

562



Table 2. Comparison of PM mass, chemical components, and intensive optical properties during long-range transported (LRT) haze and Asian dust episodes observed at Daejeon in Korea during January 2014.

	LRT haze ^a	Asian dust ^b
	Min–Max (Average \pm S.D.)	
PM ₁₀ ($\mu\text{g m}^{-3}$)	133–210 (163.9 \pm 25.0)	126–270 (211.3 \pm 57.5)
PM _{2.5} ($\mu\text{g m}^{-3}$)	100–145 (121.6 \pm 12.8)	86–147 (121.5 \pm 22.7)
PM _{2.5} /PM ₁₀ ratio	0.68–0.84 (0.75 \pm 0.06)	0.48–0.68 (0.59 \pm 0.06)
EC/PM ₁₀ ratio	0.026–0.047 (0.033 \pm 0.006)	0.023–0.032 (0.026 \pm 0.003)
K ($\mu\text{g m}^{-3}$)	0.1–1.5 (0.8 \pm 0.5)	0.02–4.9 (2.2 \pm 2.3)
$\sigma_{s,550}$ (Mm ^{−1})	358.8–594.4 (503.4 \pm 60.5)	276.1–678.4 (560.9 \pm 151)
$\sigma_{a,550}$ (Mm ^{−1})	29.3–105.4 (51.9 \pm 21.9)	29.4–46.1 (39.4 \pm 7.3)
\hat{A} (450/700)	1.30–1.47 (1.39 \pm 0.05)	0.94–1.25 (1.08 \pm 0.14)
ω_{550}	0.84–0.94 (0.91 \pm 0.03)	0.90–0.94 (0.92 \pm 0.02)

^aLRT haze: 17 January 2014, 00:00–23:00 LT

^bAsian dust: 20 January 2014, 13:00–18:00 LT



Figure captions

Fig. 1. Map of the measurement site (36.19° N, 127.24° E) in Daejeon, Korea (base map is from Google Maps).

Fig. 2. Temporal variations in (a) wind speed and hourly precipitation, (b) PM_{2.5} and PM₁₀ mass concentrations, (c) PM_{2.5}/PM₁₀ mass ratio, and light scattering coefficient (σ_s) at 450, 550, and 700 nm at the Daejeon site during January 2014.

Fig. 3. Temporal variations in (a) $\sigma_{s,550}$, (b) the Ångström exponent of σ_s (Å), (c) the backscattering fraction (b), and single scattering albedo (ω) at 450, 550, and 700 nm. Å(450/550) represents the Ångström exponent calculated from σ_s at 450 and 550 nm.

Fig. 4. Scatter plot of $\sigma_{s,550}$ versus (a) ω_{550} and (b) Å(450/700) during the entire measurement period.

Fig. 5. Scatter plots of (a) b_{550} versus ω_{550} and (b) Å(450/700) versus b_{550} as a function of $\sigma_{s,550}$.

Fig. 6. MODIS RGB images over East Asia during 14–17 January 2014.

Fig. 7. Air mass backward trajectories arriving at the measurement site on (a) 16 and (b) 20 January 2014. Red, blue, and green lines represent backward trajectories arriving at heights of 200, 500, and 1000 m, respectively.

Fig. 8. Temporal variations in (a) mass concentrations of PM_{2.5} chemical components and (b) PM_{2.5} mass fractions of major components during 14–17 January 2014.

Fig. 9. Temporal variations in (a) daily average Å(450/700) and b_{550} , (b) mass scattering efficiency at 550 nm (MSE_{550}), and (c) ω_{550} during 14–17 January 2014.

Fig. 10. Scattering efficiency of (NH₄)₂SO₄ and organic aerosols as a function of



594 particle diameter, as calculated from Mie theory.

595 Fig. 11. Comparison of (a) average $\sigma_{s,550}$ during the severe long range transported haze

596 episode (17 January) and during the Asian dust episode (20 January). Comparisons

597 of $\tilde{A}(450/700)$, b_{550} , and ω_{550} are shown in (b), (c), and (d), respectively.

598



Figure 1

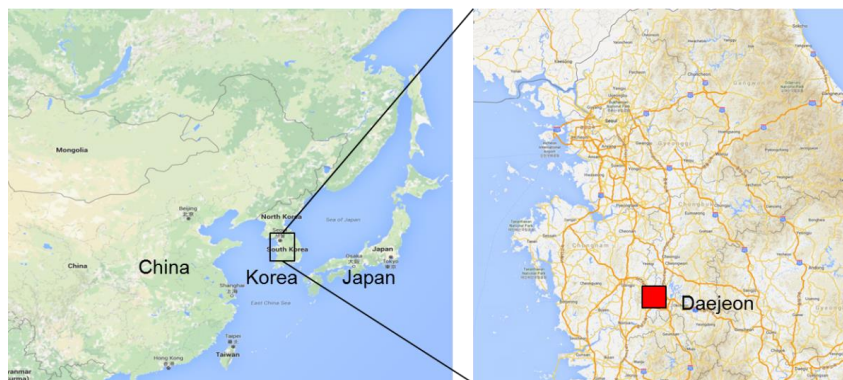




Figure 2

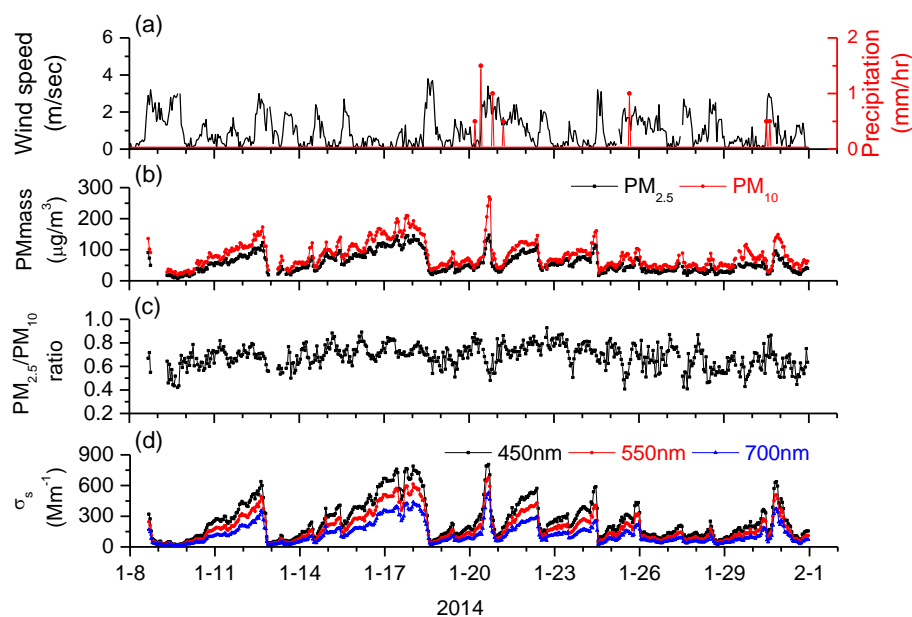




Figure 3

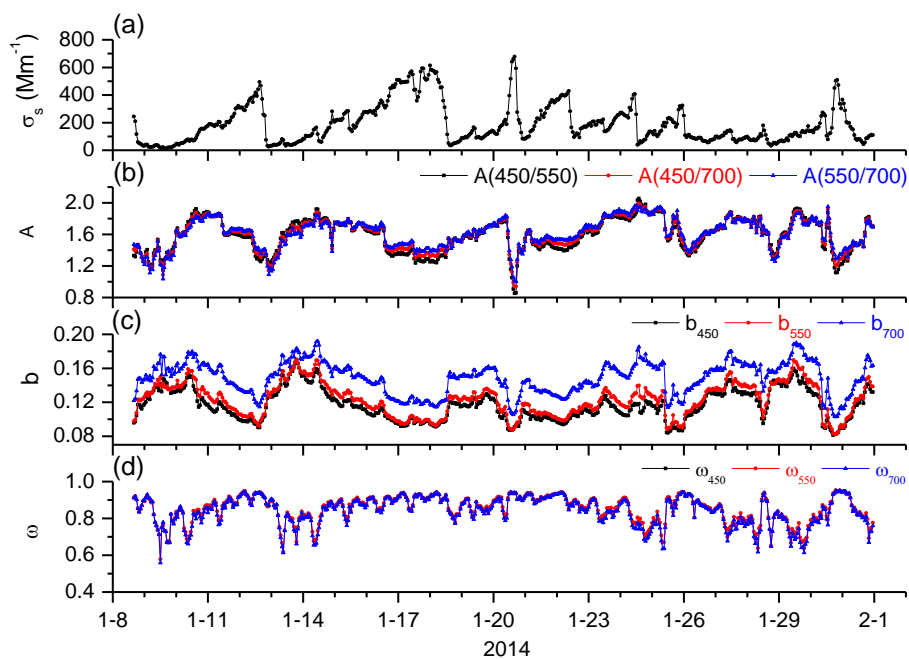




Figure 4

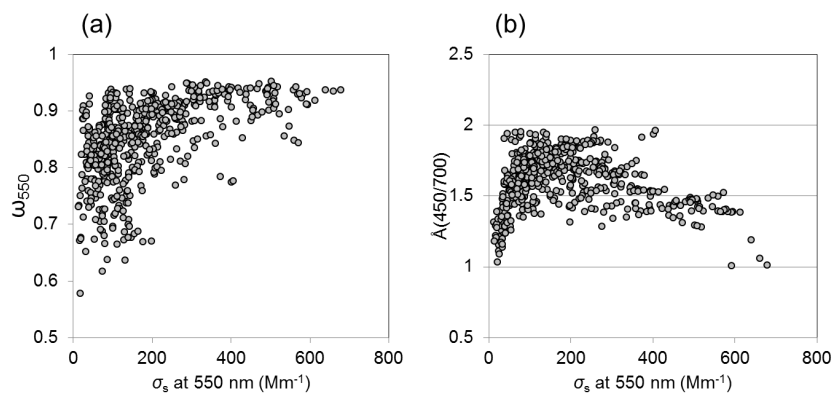
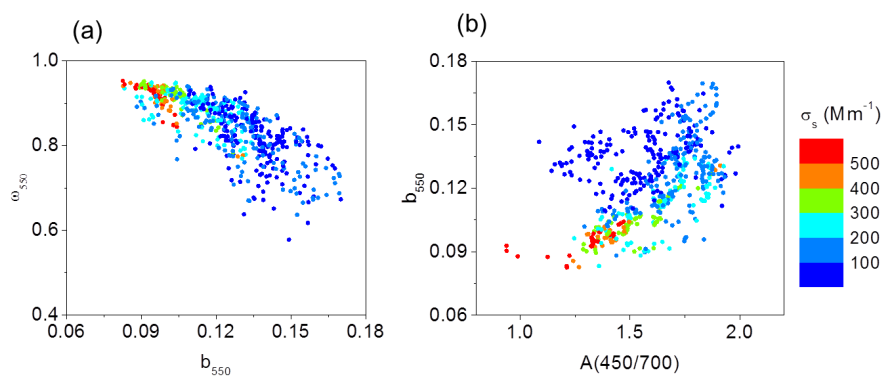




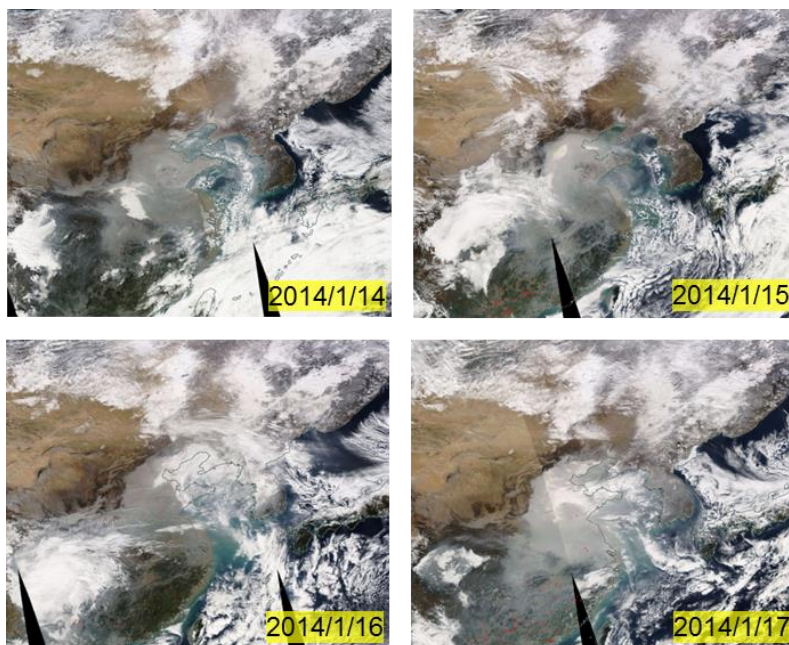
Figure 5





619
620

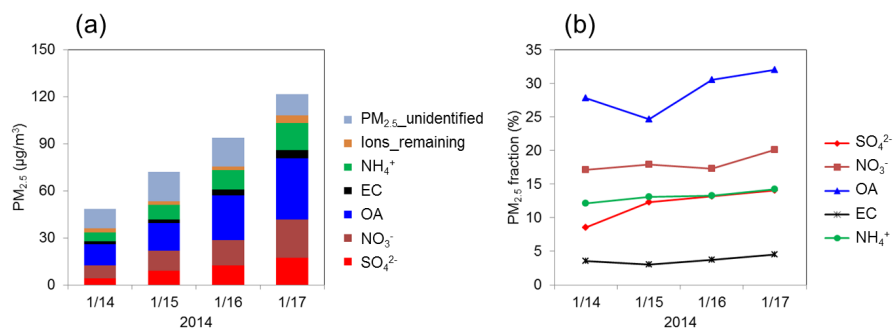
Figure 6



621
622



Figure 8

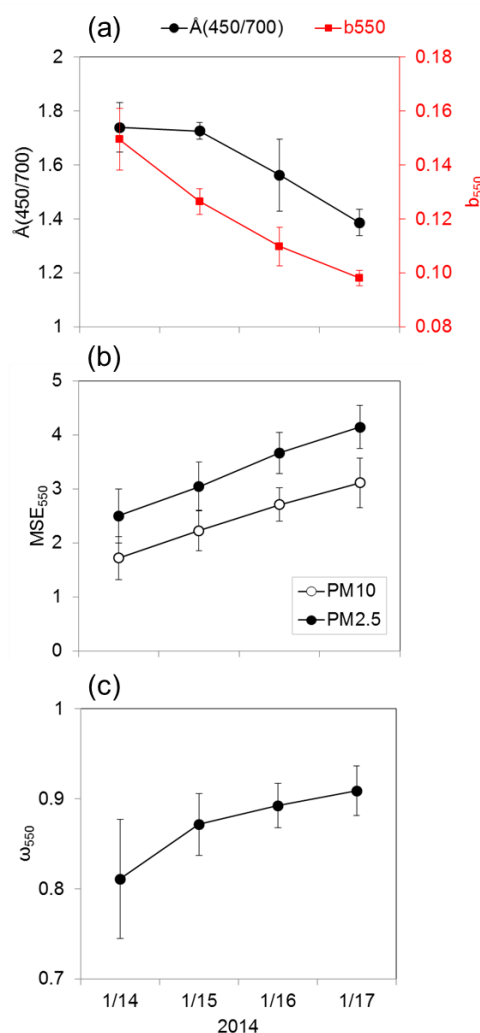




631

632

Figure 9

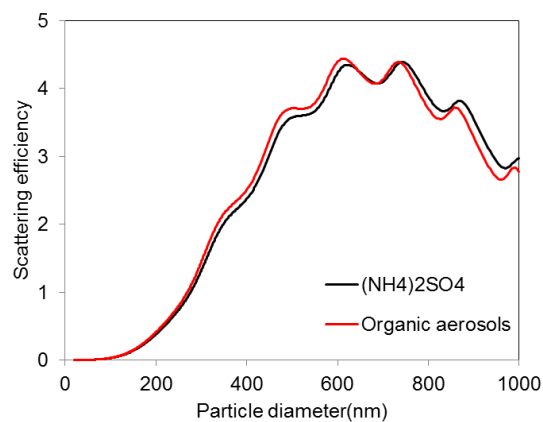


633



634
635

Figure 10



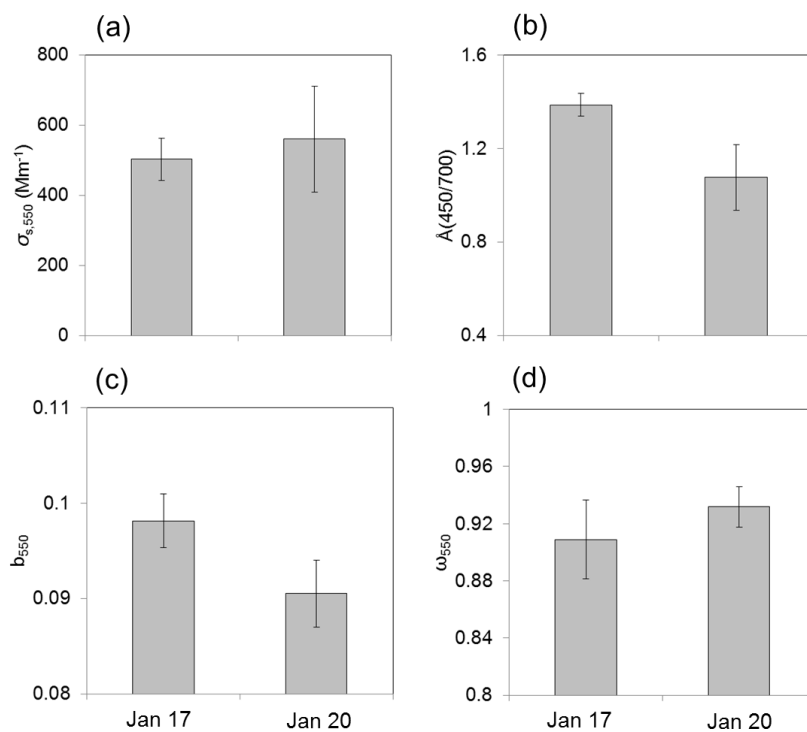
636
637



638

Figure 11

639



640

641